

A Micromagnetic Study of Magnetization Reversal in Ferromagnetic Nanorings.

Gabriel D. Chaves-O'Flynn,^{*} A.D. Kent,[†] and D.L. Stein[‡]

Department of Physics, New York University, 4 Washington Place, New York, New York 10003, USA

We present results of micromagnetic simulations of thin ferromagnetic rings undergoing magnetization reversal. This geometry is one of few examples in micromagnetics in which the transition states have been found analytically in a 1D model. According to this model, at low fields and large ring sizes, the energetically preferred transition state is a localized magnetization fluctuation (instanton saddle). At high fields and small ring size, the preferred saddle state is a uniformly rotated magnetization (constant saddle). In the first part of this paper, we use numerical micromagnetic simulations to test these predictions of the 1D analytical model for more realistic situations, including a variety of ring radii, annular widths and magnetic fields. The predicted activation energies for magnetization reversal are found to be in close agreement with numerical results, even for rings with a large annular width where the 1D approximation would be expected to break down. We find that this approximation breaks down only when the ring's annular width exceeds its radius. In the second part, we present new metastable states found in the large radius limit and discuss how they provide a more complete understanding of the energy landscape of magnetic nanorings.

I. INTRODUCTION

The magnetic properties of thin ferromagnetic annuli have attracted attention due to their potential applications in magnetic random access memory: the absence in such geometries of edges or corners to nucleate magnetization reversal leads to greater stability against reversal than in other simply connected thin film elements.

There are several ways in which ferromagnetic annuli may be used as memory elements, differing in the (meta)stable magnetization configurations that represent a single bit. In all of these the magnetization lies completely within the plane and its configuration is smooth everywhere. One such pair of configurations is of opposite chirality, i.e., clockwise or counterclockwise circulation of the magnetization^{1,2,3}; another is the so-called "onion states"^{4,5,6,7,8,9}, where there is a net total magnetization along a direction in the ring's plane. In the former (latter) case, a circumferentially (uniformly) directed magnetic field can be used to set the magnetization configuration. The minimum energy configurations depend on the strength and direction of the magnetic field as well as the relative dimensions of the ring with respect to the exchange length.

Few analytic solutions have been obtained for the rate of thermally induced reversal in micromagnetic problems, even in relatively simple geometries. For thin annuli under the influence of a circumferential magnetic field, however, the lowest energy transition (or saddle) states have been found analytically¹⁰ in a one-dimensional approximation and studied numerically in the full three-dimensional problem¹¹.

The Kramers theory of reaction rates¹² can be used to compute the typical lifetime of a given state when

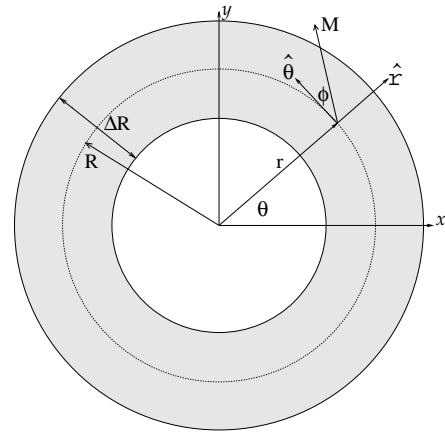


Figure 1: Ring geometry showing the coordinates. The current runs along the axis of the ring out of the page.

there are several minimum energy configurations. The general form for the rate Γ of thermally induced transitions between two minima in the limit of low noise is given by the well-known Arrhenius formula¹³ $\Gamma = \Gamma_0 \exp(-\Delta E/k_B T)$, where the prefactor Γ_0 is usually independent of the noise strength and depends only on the shape of the energy landscape close to the extremal states relevant to the transition. The activation energy, ΔE , equals the energy difference between the transition state and the metastable state, thereby determining the stability of the latter. This is an important figure of merit for memory devices.

In this paper, numerical micromagnetics are used to test the predictions of the analytical theory of Martens et al.¹⁰ for thermally induced transitions between states of opposite chirality in a 1D approximation to the annular ring. The simulations were made for a variety of mean radii, annular widths and magnetic fields.

The geometry under study and accompanying relevant parameters are represented in Fig. 1. The magnetic material is in the shape of an annulus of mean radius R , an-

^{*}Electronic address: gdc229@nyu.edu

[†]Electronic address: andy.kent@nyu.edu

[‡]Electronic address: daniel.stein@nyu.edu

nular width ΔR and (in the third dimension) thickness t . A current I running along the axis of the ring produces a circumferential external field $\mathbf{H}(r) = (I/2\pi r)\hat{\theta}$. The ring is composed of a soft isotropic ferromagnet (e.g., permalloy) with saturation magnetization M_s and exchange length λ . In all of the geometries considered, the aspect ratio $k = t/R \ll 1$, giving rise to magnetostatic forces that constrain the magnetization to lie in the plane of the ring ($M_z = 0$)¹⁰. A magnetization configuration can therefore be completely described by $\phi(\theta, r)$, the angle the magnetization at a given radius makes with the unit vector lying along the tangent to the circle with that radius: $\mathbf{M}(\theta, r) = (M_x, M_y, M_z) = M_s(\sin(\phi - \theta), \cos(\phi - \theta), 0)$.

II. MODEL

Our starting point is the Landau-Lifshitz-Gilbert (LLG) equation^{14,15}

$$\frac{d\mathbf{M}}{dt} = -|\gamma|\mathbf{M} \times \mathbf{H}_{\text{eff}} - \frac{|\gamma|\alpha}{\mathbf{M}_s}\mathbf{M} \times (\mathbf{M} \times \mathbf{H}_{\text{eff}}), \quad (1)$$

where γ is the gyromagnetic ratio and α is the (phenomenological) damping constant. The effective magnetic field, $\mathbf{H}_{\text{eff}} = -\nabla_{\mathbf{M}}E$, contains all (external and internal) fields and is the variational derivative of the total micromagnetic energy

$$E[\mathbf{M}(\mathbf{r})] = \frac{\mu_0\lambda^2}{2} \int_{\Omega} d^3r |\nabla\mathbf{M}|^2 + \frac{\mu_0}{2} \int_{\mathbf{R}^3} d^3r |\nabla U|^2 - \mu_0 \int_{\Omega} d^3r \mathbf{H}_e \cdot \mathbf{M}. \quad (2)$$

The three terms above correspond respectively to the exchange energy, demagnetization (or magnetostatic) energy, and Zeeman energy, with the (small) magnetocrystalline anisotropy term neglected. (The last of these can be easily included, but for the materials and geometries considered here, it is typically overwhelmed by the much larger shape anisotropy arising from the demagnetization term.) Here Ω is the volume of the ring, $\lambda = \sqrt{2A/(\mu_0 M_s^2)}$ is the exchange length (where M_s , the magnitude of the magnetization, is assumed to be the same everywhere, and A is the exchange constant), \mathbf{H}_e is the applied external magnetic field, and $|\nabla\mathbf{M}|^2 \equiv |\nabla M_x|^2 + |\nabla M_y|^2 + |\nabla M_z|^2$. The ‘‘magnetostatic potential’’ U , arising from long-range dipole-dipole interactions within the magnetic material, satisfies $\nabla^2 U = \nabla \cdot \mathbf{M}$ (and suitable boundary conditions in the interfaces between media), which can be derived through Maxwell’s equations. Our simulations involve numerical integration of the above set of equations.

The extremal states of a quasi-1D ferromagnetic ring (i.e., $\Delta R \ll R$ so that the external magnetic field does not vary significantly with distance from the center of the ring) in a circumferential magnetic field have been analytically obtained¹⁰. The solutions found there apply in the thin-ring limit: $k = t/R \ll 1$ and $(\lambda/R)^2 \sim$

$(t/R)|\ln(t/R)|$. Under these conditions the second term on the RHS of (2) separates into three main terms (and a number of smaller ones): a term which extracts a large energy cost when the magnetization does not lie completely within the plane of the annulus; a local surface term (the shape anisotropy, which favors alignment of the magnetization with the tangential direction at the inner and outer ring radius); and a nonlocal bulk contribution. Analysis of these terms finds that the bulk term is small compared to the surface term and can therefore be neglected¹⁰. In Sec. IV we test these conclusions for more realistic geometries by computing numerically the *total* demagnetization energy and comparing it to the (analytically computable) local surface (i.e., shape anisotropy) term.

In the 1D approximation the total energy reduces to

$$E = 2\mu_0 M_0^2 \left(\frac{\ell}{2\pi}\right)^2 \frac{t}{R} + \lambda^2 \int_0^\pi \left[\left(\frac{2\pi}{\ell} \frac{\partial\phi}{\partial\theta}\right)^2 + \sin^2\phi - 2h \cos\phi \right] d\theta, \quad (3)$$

where the parameters ℓ and h are the scaled circumference and field:

$$\ell = \frac{R}{\lambda} \sqrt{2\pi \left(\frac{t}{\Delta R}\right) \left|\ln\left(\frac{t}{R}\right)\right|} \quad (4)$$

$$h = \frac{H_e}{H_c} = \frac{\mu_0 M_s}{\pi} \left(\frac{t}{\Delta R}\right) \left|\ln\left(\frac{t}{R}\right)\right|,$$

and H_c is defined below. The first term in the integrand is the exchange energy, the second the shape anisotropy (i.e., the surface term arising from the demagnetization energy), and the last is the Zeeman term.

Given an external magnetic field that is circumferential and points everywhere in the counterclockwise direction, there are two states that are local minima of the energy: a stable magnetization configuration (ground state), which is everywhere aligned with the external field, and a metastable state that is everywhere antiparallel to the field (i.e., circumferential and pointing everywhere in the clockwise direction). H_c corresponds in eq. 4 to the magnetic field at which the metastable configuration becomes unstable.

There are also two relevant unstable stationary configurations (i.e. saddle states). These are defined by the angle ϕ that the magnetization direction makes with the circumferential direction at each point in the annulus; i.e., ϕ is a function of the angle θ (as shown in Fig. 1), $\phi_{\ell,h}(\theta)$. In the limit of low noise, reversal of the magnetization occurs through the lower energy saddle state. One of these corresponds to a global rotation of the magnetization in which ϕ is independent of θ ; we therefore label it the ‘‘constant saddle’’, and is denoted ϕ_h . The constant saddle favors the exchange and Zeeman energies at the expense of the demagnetization energy. The second saddle state is a localized fluctuation of the magnetization and we therefore refer to it as the ‘‘instanton saddle’’, and denote it by $\phi_{h,\ell}(\theta)$ (denoted as instanton saddle in¹⁰). This state favors the demagnetization energy at the expense of the exchange and Zeeman energies.

Which of these two saddles is energetically favored depends on the applied field and the ring size. When the scaled field h is smaller than $\sqrt{1 - (2\pi/\ell)^2}$ the instanton saddle has a lower energy than the constant saddle; otherwise, the constant saddle is lower in energy. Fig. 2 of¹⁰ shows the phase boundary between the two activation regimes as a function of h and ℓ .

We simulated the dynamics using the analytical solutions as our initial configurations for the two saddle states:

$$\phi_h = \cos^{-1}(-h) \quad (5)$$

for the constant saddle, and

$$\phi_{h,\ell} = 2 \cot^{-1} \left(\vartheta \operatorname{dn} \left(\frac{\theta \mathbf{K}(m)}{\pi} |m \right) \right) \quad (6)$$

for the instanton saddle. Here $\operatorname{dn}(\cdot|m)$ is the Jacobi elliptic function with $0 \leq m \leq 1$, and $\mathbf{K}(m)$ is the complete elliptic integral of the first kind¹⁶. The parameter m satisfies,

$$\frac{\ell}{2\mathbf{K}(m)} = \frac{m}{\sqrt{2 - m - \sqrt{m^2 h^2 + 4(1 - m)}}} \quad (7)$$

and ϑ is defined by,

$$\vartheta = \sqrt{\frac{2 - mh - \sqrt{m^2 h^2 + 4(1 - m)}}{2m - 2 + mh + \sqrt{m^2 h^2 + 4(1 - m)}}}. \quad (8)$$

For sufficiently small rings ($\ell \leq 2\pi$), the instanton saddle does not exist (essentially, the variation of the magnetization, which is of order the exchange length, cannot “fit” onto the ring). In this limit $m \rightarrow 0$ and the instanton solution reduces to the constant saddle. As the ring becomes larger the parameter m increases from 0 to 1 monotonically with ℓ . For $\ell \gg 2\pi$ the m becomes numerically indistinguishable from 1. In this limit the instanton saddle configuration is given by:

$$\phi_{h,\ell} = 2 \tan^{-1} \left(\sqrt{\frac{h}{1-h}} \cosh \left(\frac{\theta \ell}{2\pi} \sqrt{1-h} \right) \right). \quad (9)$$

We classify rings according to their ℓ values as small ($\ell \leq 2\pi$), medium ($\ell \gtrsim 2\pi$), and large ($\ell \gg 2\pi$). Physically, ℓ characterizes the ratio of the magnetostatic to exchange energies. A medium ring ($\ell \gtrsim 2\pi$) has a scaled circumference close in size to a domain wall in the material. The saddle configurations of each regime are shown in Fig. 2.

The activation energies within the 1D analytical model can be calculated using 3(cf.¹⁰). For the constant saddle they can be analytically computed: $\Delta E = \mu_0 M_0^2 t^2 R |\ln(t/R)|(1-h)^2$.

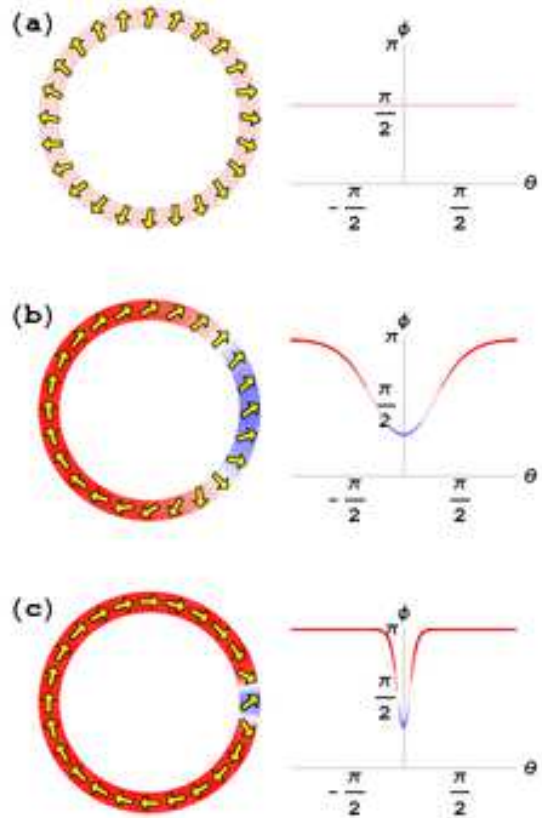


Figure 2: Saddle configurations computed analytically from the 1D model of Martens *et al.* for small, medium and large ring sizes. a) For small rings the magnetization reversal goes through the constant saddle state; b) when $\ell > 2\pi$ the transition is via the instanton saddle; c) as the relative size of the ring increases the fluctuation in the instanton saddle occupies a smaller fraction of the ring.

III. METHOD

We studied thin nanorings by running simulations on the model of Sect. II using the publicly available packages OOMFF and Nmag^{17,18}. These packages effectively simulate the dynamics specified by (1) and (2) at zero temperature; i.e., all runs start from an initial configuration and run downhill in energy.

Our initial states were the instanton and constant saddles described by (5) and (6), which provided starting points that were guessed to be relatively close to the actual saddles. The system subsequently relaxed to the actual saddle states, which turned out to be remarkably close to analytical solutions. We describe below how this was determined.

Depending on the starting state, the system will evolve to one or the other (meta)stable state, i.e., either the clockwise or the counterclockwise magnetization configu-

ration. In order to find the actual 2D saddle numerically (recall that the magnetization is forced by the magnetostatic energy term to lie in the plane of the ring), we introduce a new field value, denoted h_t , an “effective field” for which the state $\phi_{h,l}$ behaves as a saddle state. In determining h_t , two criteria are used. First, $\phi_{h,l}$ must be as nearly a stationary state as the numerics allow, i.e., the initial time derivative of the total micromagnetic energy should be close to zero ($\lim_{h_e \rightarrow h_t} \frac{\delta E}{\delta t} \Big|_{t=0} \rightarrow 0^-$). Second, the state $\phi_{h,l}$ should mark the boundary between the basins of attraction of each (meta) stable state (i.e., for $h < h_t$ the system evolves to a clockwise state, while for $h > h_t$, it evolves to the counterclockwise state). In the following sections, we show that these criteria are satisfied in a variety of rings with different exchange lengths and annular widths. We also show how the model eventually breaks down when the width of the ring becomes very large.

The procedure can be summarized as follows. For a given initial $\phi_{h,l}$ we find the appropriate h_t by a bracket and bisection iterative process. We set the initial configuration $\phi_{h,l}$, fix the external magnetic field at the value h_e and allow the system to relax. If the final state is the metastable (clockwise) configuration we increase h_e by an amount δh_e ; if the final state is the stable (counterclockwise) configuration we decrease h_e by δh_e . We then start a new run and reduce δh_e by a factor of 2. As δh_e decreases, the total relaxation time increases due to the slow dynamics at the start of the simulation, providing evidence that the initial configurations are approaching the true saddle states. We iterate until we reach a numerical uncertainty of $\delta h = 6 \times 10^{-3}$.

The Nmag simulations were run using a mesh consisting of 20963 volume elements, 15154 surface elements, and 7594 points with an edge length of average 3.89 nm and standard deviation of 0.7. (The quality distribution of the mesh was 1.66% below 0.6; 9.11% between 0.6 and 0.7, 57.28% between 0.7 and 0.8, 32.05% between 0.8 and 0.9, and 0.01% above 0.9.) The cell sizes for the simulations in OOMMF were selected so that they were smaller than the exchange length for each of the regimes studied. Different values of ℓ for a given geometry were studied by changing the exchange constant A (cf. below (2)) and keeping the ring dimensions constant. This changes λ and therefore ℓ , the mesh can be adjusted to speed up the simulations.

A. String Method in Rare Events

The String Method¹⁹ is a recently introduced numerical procedure for calculating transition energies and paths within the context of large fluctuations and rare events. It is useful to find the path connecting two stable configurations \mathbf{M}_A and \mathbf{M}_B , through a curve ξ with minimum energy. The obtained path corresponds to the reversal trajectory in the limit where the precession term of (1) is negligible compared to the damping term. This

curve ξ satisfies

$$\nabla_{\mathbf{M}} E^\perp(\xi) = \nabla_{\mathbf{M}} E(\xi) - [\nabla_{\mathbf{M}} E(\xi) \cdot \hat{t}] \hat{t} = 0 \quad (10)$$

where \hat{t} is the unit tangent of the curve ξ . The curve ξ is found by guessing a parametrized path $\xi(0) = \{\mathbf{M}(\alpha) \in [0, 1], \mathbf{M}(0) = \mathbf{M}_A, \mathbf{M}(1) = \mathbf{M}_B\}$ and evolving it in “time” according to:

$$\partial_t \mathbf{M}(\alpha) = -\nabla_{\mathbf{M}} E^\perp(\mathbf{M}(\alpha)) + \lambda \hat{t}. \quad (11)$$

The second term is added to enforce a particular parametrization; it does not alter the actual evolution of the curve. It is convenient to rewrite this equation as:

$$\partial_t \mathbf{M}(\alpha) = H_{\text{eff}}^\perp(\mathbf{M}(\alpha)) + \lambda \hat{t} \quad (12)$$

For numerical purposes the path ξ is discretized with $N+1$ points between \mathbf{M}_A and \mathbf{M}_B . After each iteration of (12) with an Euler forward algorithm the magnetization vectors are renormalized to \mathbf{M}_s . In Sect. VI we use this method to find the barrier between two states connected through a transition state.

IV. MEDIUM SIZE NARROW RING

We consider a narrow ring of medium reduced circumference ℓ (i.e., the parameter m not close to 1) with $\lambda/R \ll 1$, $t/R \ll 1$ and $(\lambda/R)^2 \sim (t/R) |\ln(t/R)|$ ($A = 3.2 \times 10^{-10}$ J/m, $\Delta R = 40$ nm, $R = 200$ nm, $t = 2$ nm, $M_s = 8 \times 10^5$ A/m). With these values, ℓ and H_c are 12 and 73.9 mT, respectively. We first test numerically whether the surface, or shape anisotropy, term is in fact the main contributor to the magnetostatic energy, as required for the validity of the analytic solutions to hold¹⁰. Using OOMMF and Nmag the total demagnetization energy were obtained for different values of h and compared to the values of the surface term (second term in the integrand of (3)). The results of this comparison are presented in Fig. 3, which

shows that the numerical computation of the total demagnetization energy gives nearly the same dependence on h as the contribution from the shape anisotropy alone. This provides numerical support for the approximations used to arrive at the 1D analytical solutions of¹⁰ and confirms that the bulk magnetostatic term, neglected in the analytic model, is indeed not important.

We also compare the total demagnetization energies computed using OOMMF for different cell sizes in Fig. 3b. Three suitable methods to calculate the demag energy are available in the OOMMF package; ConstMag, 3dSlab, 3dCharge. Constmag calculates the average demagnetization field assuming the magnetization is constant in each cell; 3dSlab uses a demag field obtained from blocks of constant charge; and 3dCharge uses constant magnetization to calculate the in-plane component

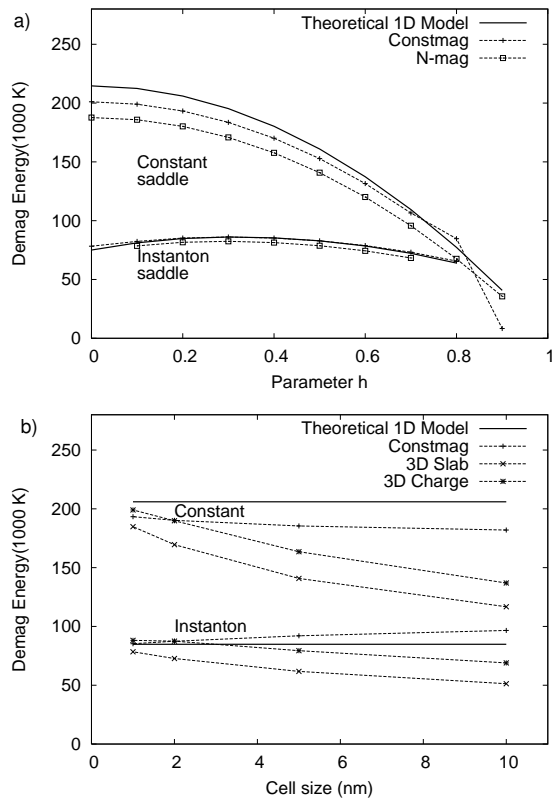


Figure 3: Total demagnetization energies, using different calculation methods, compared to analytical results for the shape anisotropy term alone ($A = 3.2 \times 10^{-10}$ J/m, $R = 200$ nm, $t = 2$ nm and $\Delta R = 40$ nm). a) Comparison of OOMMF using the ConstMag method at cell size 1 nm and Nmag with theoretical predictions vs. h . b) Demagnetization energy vs. cell size using three different methods for computing this energy in OOMMF, all for $h = 0.2$. The solid line is the analytical computation of the shape anisotropy term alone.

of the magnetic field, and constant charges to calculate the out of plane demagnetizing field. As seen in the figure, the consistency between different methods of calculation improves as cell size is reduced; and the numerical results approach that of the 1D model.

Once h_t is obtained following the method described in Sect. III, the saddle state is numerically obtained and the activation energy is thereby determined from the difference between each saddle state and the metastable state. Fig. 4 displays curves at $h_t = 0.21$ for each of the two saddle states used as initial configurations.

As can be seen in the figure, after a very short transient the system arrives at a configuration in which the energy stays almost constant for an extended period; this indicates that the initial 1D analytical solution is close in both energy and its geometrical configuration to the true 2D saddle. Eventually, the saddle state decays into one of the two stable configurations. The activation energy is easily computed this way (as seen in Fig. 4), and a glance at the figure confirms that for the applied field $h_t = 0.21$

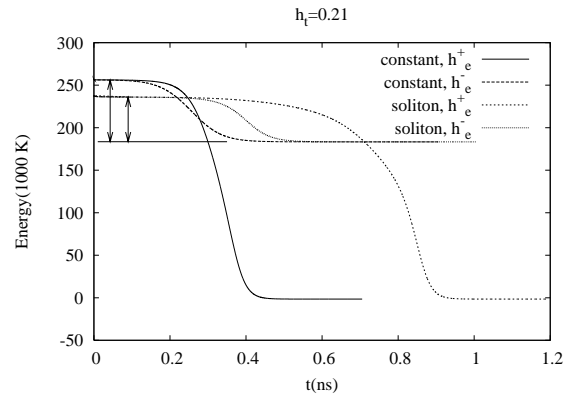


Figure 4: Evolution of the total micromagnetic energy with time. Arrows show activation energy of each saddle. The configurations shown bifurcates at the fields given and have an initial slow evolution. The two criteria used to determine a saddle state.

the instanton configuration has a lower activation energy than the constant saddle, as predicted theoretically¹⁰.

The method described in Sect. III was repeated to obtain the behavior of ΔE as a function of h_t . Using this approach one can calculate $h_t \approx \frac{h_e^+ + h_e^-}{2}$ and $\Delta E = \frac{E[\phi_h, h_e^+] + E[\phi_h, h_e^-]}{2} - E[\phi = \pi, h_t]$ for each of the two saddle configurations. Here, $E[\phi_h, h_e]$ represents the numerical energy of a configuration ϕ_h under an applied field of magnitude h_e . The results are summarized in Fig. 5 together with the analytical predictions.

Figs. 5a and 5b show $\Delta E(h_t)$ for the instanton saddle and constant saddle, respectively. From bottom to top the curves represent calculations in OOMMF for two different cell sizes, an Nmag calculation and the analytical prediction.

The Nmag results are closer to the analytical predictions than the OOMMF calculations. This is due to the fact that the curvature is more faithfully represented by a mesh of tetrahedrons in Nmag, whereas OOMMF represents the ring with a square grid. The edges of the tetrahedrons can be arranged to follow closely the curvature of the ring, whereas the square cells edges will in most cases make a finite angle with the ring tangent. This results in a much larger error contribution to the demagnetization energy in square grids in OOMMF than in Nmag.

Fig. 5c presents the Nmag simulation results for the activation energy. As predicted in Ref.¹⁰, the instanton saddle configuration is preferred at lower fields. For a fixed ℓ the activation energy curves are predicted to cross at $h_c(\ell) = \sqrt{1 - (2\pi/\ell)^2}$. For higher fields, the constant configuration is the sole saddle state (this is in contrast to the low-field side, where both solutions exist but the constant saddle has higher energy). Numerically, the field at which the crossover between the saddles occurs is somewhat lower than that predicted. This discrepancy arises because the theoretical model applies

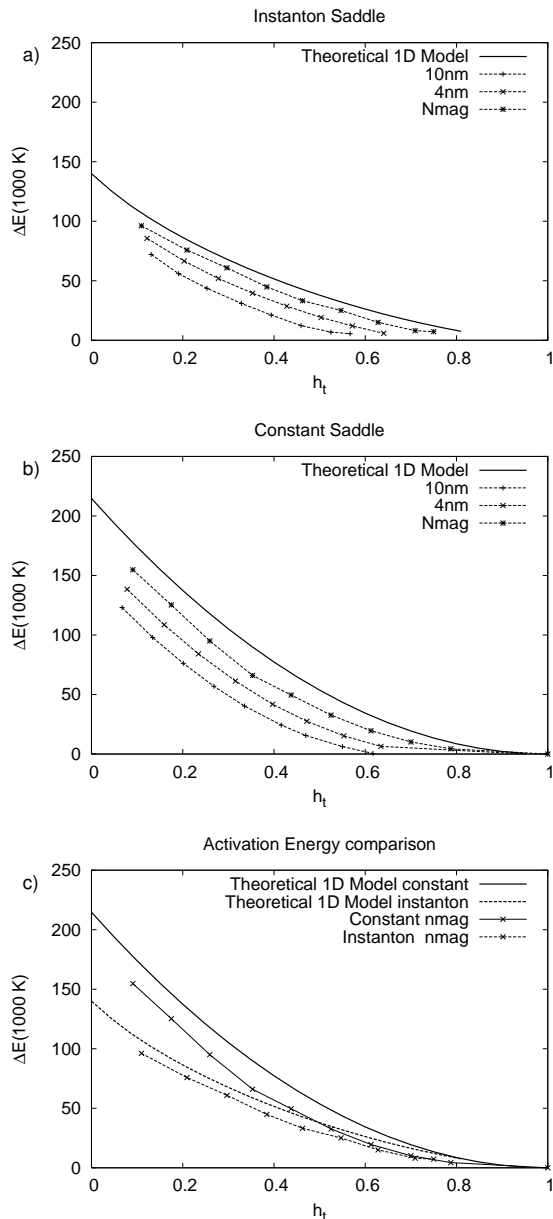


Figure 5: Comparison of the activation energies for the (a) instanton and (b) constant saddles. Data points represent steps of 0.1 in h . As the numerics are refined both by using Nmag and by reducing the cell size in OOMMF simulations the results approach the theoretical predictions. (c) Comparison for Nmag for the middle size, narrow ring ($\ell=12$, $\Delta R=40$ nm) of the corresponding curves shown in (a) and (b).

to a strictly 1D ring, whereas the simulations run using higher-dimensional rings (2D in OOMMF and 3D in Nmag).

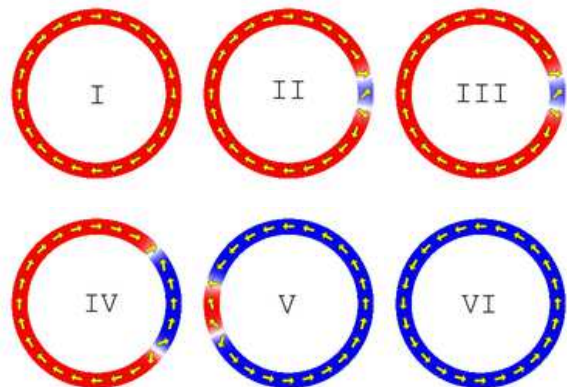
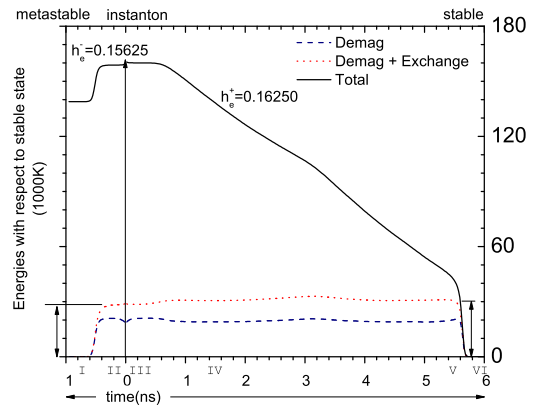


Figure 6: Evolution of the total energy with time for the instanton saddle, with energies measured with respect to that of the stable state. The decay to the metastable state is shown as proceeding to the left of $t = 0$, and to the stable state to the right of $t = 0$. The ring dimensions are $\Delta R = 40$ nm, $\ell = 60$. When $h_e < h_t$ the instanton saddle (II close to $t=0$) decays quickly into the metastable configuration (I at $t=0.7$ ns); domain walls are annihilated. When $h_e > h_t$ the two domain walls of the instanton saddle (III, close to $t=0$) separate (IV, $t=1.5$ ns), move to the opposite side of the ring (V, $t=5.4$ ns) and annihilate (VI, $t=5.7$ ns).

V. LARGE SIZE NARROW RING

We now investigate an annular film with the same dimensions but different λ (e.g., permalloy with $A = 1.3 \times 10^{-11} J/m$); the rest of the dimensions are kept the same as above. Such a ring belongs to the large ring regime ($\ell = 60$, $m \approx 1$). As before, we can obtain a qualitative understanding of the reversal process by following the time evolution of the micromagnetic energy; this is presented in Figs. 6,7. Using the fact that an instanton is a superposition of two domain walls with opposite chirality (Fig. 10b)²⁰, the features observed in Figs. 6, 7 can be explained and an intuitive idea of the reversal mechanism developed.

We begin by discussing the evolution of energy with time as shown in Fig. 6a. For $h_e < h_t$ the instanton decays into the metastable state with a rapid decrease in

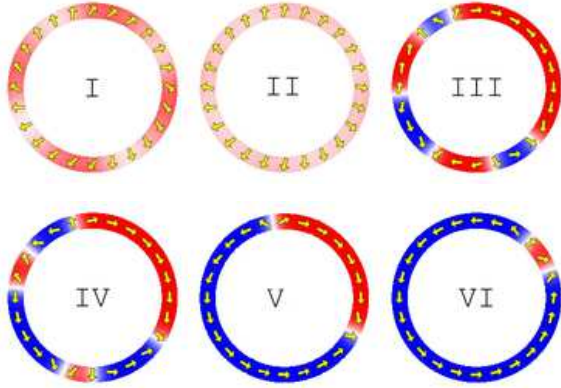
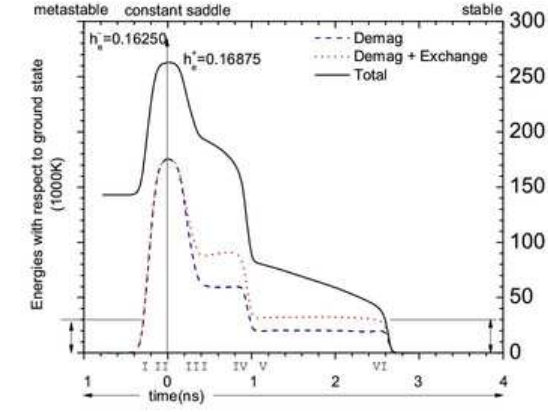


Figure 7: Evolution of the total energy with time for the constant saddle, with energies measured with respect to that of the stable state. The decay to the metastable state is shown as proceeding to the left of $t = 0$, and to the stable state to the right of $t = 0$. The ring dimensions are $\Delta R = 40$ nm, $\ell = 60$. When $h_e < h_t$ the constant saddle (II at $t=0.15$ ns) starts to decay into the metastable configuration (I at $t=0.28$ ns), it is possible to see that this decay is not uniform in all the ring, and some regions decay faster than others. When $h_e > h_t$ the constant saddle quickly develops domains (III at $t=0.51$ ns). Counterclockwise domains expand at the expense of clockwise domains (IV, $t=0.83$ ns), with annihilation that produce a sudden decrease in energy (V, $t=1.03$ ns) leaving a single domain wall pair which continues moving (VI, $t=2.52$ ns) until eventual annihilation; the slope during the last stage is very close in magnitude to the slope of Fig. 6 during domain wall propagation, the discrepancy is due to the difference of applied fields.

energy (seen to the left of $t = 0$). This corresponds to the annihilation of two transverse domain walls. The field in this case is not sufficient to separate the two transverse walls. When $h_e > h_t$ (right side) the energy of the system decays linearly with time towards the stable state and then sharply decreases. The linear time decay corresponds to movement of the transverse domain walls in opposite directions (due to the external field) at approximately constant speed as can be seen in Fig. 6. The final, sharp decrease in energy results from the col-

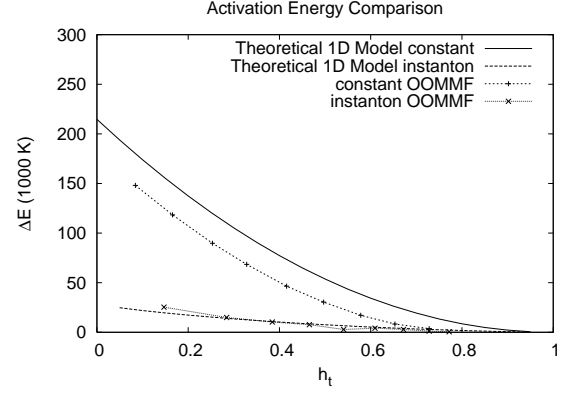


Figure 8: Total energies of the two saddle states for dimensions $\Delta R = 40$ nm, $\ell = 60$ with respect to the clockwise configuration.

lision and annihilation of the walls. Note that the magnetostatic and exchange energies remain almost constant while the walls are propagating (roughly) independently of each other. The annihilation energies of the domain walls (indicated by the arrows in Fig. 6a) are roughly the same magnitude.

The slope of the $E(t)$ curve during the propagation phase provides a measure of how fast the reversal proceeds. For the particular damping parameter used, this can be used to estimate the wall speed from the last term of (3) to be $v = \frac{1}{8n\mu_0 M_0^2} \left(\frac{2\pi}{\ell}\right)^2 \frac{R^2}{\lambda^2 t} \left\langle \frac{dE}{dt} \right\rangle$ where n is the number of domain wall pairs present in the ring. In deriving this expression $\phi = 0, \pi$ for each domain and domain widths are assumed to remain constant during propagation. A comparison to medium-sized rings shows that at fixed h the reversal time increases as λ decreases for two reasons: the domain wall width is comparatively smaller and the effective scaled circumference ℓ is comparatively larger (cf. Figs. 4 and 6).

The time dependence of the energy for the constant saddle case, Fig. 7, is seen to proceed in several steps where the energy decrease is gradual, punctuated by large changes in the slope dE/dt . These features can be explained as follows. Fig. 8 shows that the activation energy of the constant saddle at $h \approx 0.17$ is several times larger than the activation energy of the instanton saddle at the same field. With such a large activation energy, it is relatively easy to create several domain wall pairs along different (randomly placed) parts of the ring, each of them with an energy cost roughly equal to the activation energy of the instanton. In the simulations, this process is modified by the discretization of the ring, and in an experimental setup it is possible that impurities and edge roughness might play a similar role. The abrupt changes in slope are due, as before, to the annihilation of domain wall pairs and hint at a richer spectrum of states that are stationary in the energy when the scaled circumference is large compared to the exchange length.

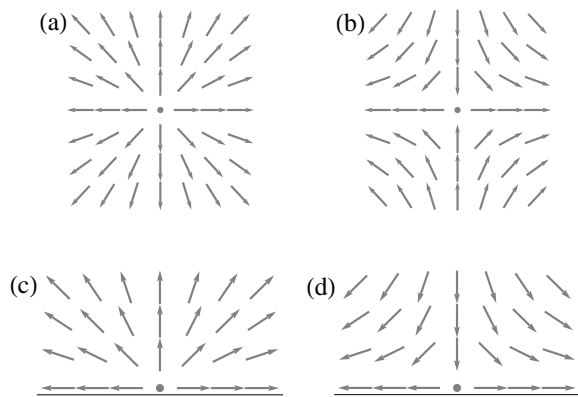


Figure 9: Topological defects of the XY model in the bulk (a,b) and in the presence of an edge (c,d), with winding numbers of 1,-1,+1/2,-1/2 respectively.

A. Multiple Wall Pair Spectra

We have also gone beyond the work of Martens *et al.* by finding numerically new stable states consisting of multiple domain wall pairs. When present, these states influence the time evolution of the system in a manner similar to that just described. In this section we discuss these new states and present a model to incorporate their effects on magnetization reversal.

Fig. 10d shows one of these locally stable double pair states. They can be described as a combination of topological defects, in particular edge defects and domain walls, which we will now describe (cf. Fig. 9). Bulk topological defects are vortex and antivortex singularities of the magnetization configurations with a net contribution to the exchange energy²¹. They are characterized by their winding number which is conserved over any continuous transformation of the magnetization. Close to an edge of the material the singularities become *half-vortices* with winding number $\pm 1/2$ ²². Since $\ell \rightarrow \infty$ for the limit $m \rightarrow 1$, we can consider any small segment of the ring as a strip: the outer edge of the ring maps into the lower part of the strip.

A transverse domain wall can be described as a composite of two edge defects of opposite sign²² at opposite sides of a ferromagnetic strip (see Fig. 10a). In the ring, it is convenient to label such a domain wall using the sign of the topological defect on the inner side of the ring. The topological defects experience a “Coulomb-like” attraction or repulsion. Walls where the magnetization points in opposite directions (equal signs for same side edge defects as in Fig. 10c) experience repulsive interactions. The origin of repulsion arises from the magnetostatic and exchange energies in the region between walls. Walls which are parallel to each other (with opposite signs in the same side edge defects, as in Fig. 10b) experience attractive interactions.

Any small fluctuation of the magnetization initially

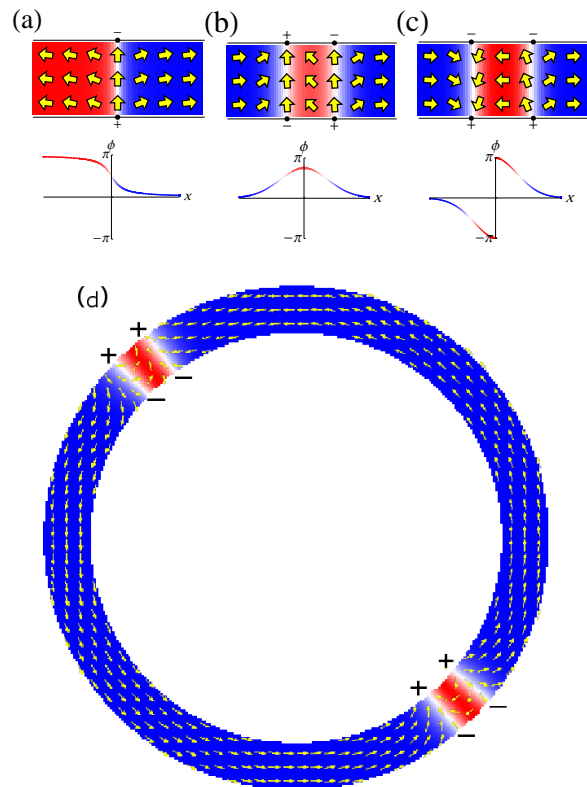


Figure 10: a) Transverse domain wall composed of two edge defects of opposite sign. b) Magnetic configuration equivalent to the instanton state in a stripe. c) A trapped domain state configuration between two antiparallel walls. d) Low energy metastable state configuration. The topological defect sign at the inner boundary determines if the domain wall pairs are stable with respect to the external magnetic field. With respect to the ground state (counterclockwise), this state has a winding number of zero, as do the instanton saddle, constant saddle and clockwise configurations.

parallel to the ring (strip) edges would be a precursor to a double wall of this last type (Fig. 10b) as illustrated by the profile of such configurations. The radial component of the magnetization in the ring (transversal component in the strip) edges could have any sign: the fluctuation will have the same energy whether the magnetization tilts towards the inside or the outside of the ring (up or down in a strip). A reversal can be produced by a fluctuation with equal probability for any of these two orientations.

The domain between two walls will expand under the influence of a parallel external magnetic field (producing a repulsive pressure on the walls), and contract under an antiparallel magnetic field (producing an attractive pressure on the walls). The balance between the interdefect interaction and the field determines whether a configuration is in stable or unstable equilibrium. For example, an instanton saddle configuration is equivalent to two domain walls with opposite signs on their innermost defects which enclose a domain parallel to the field (cf. signs in

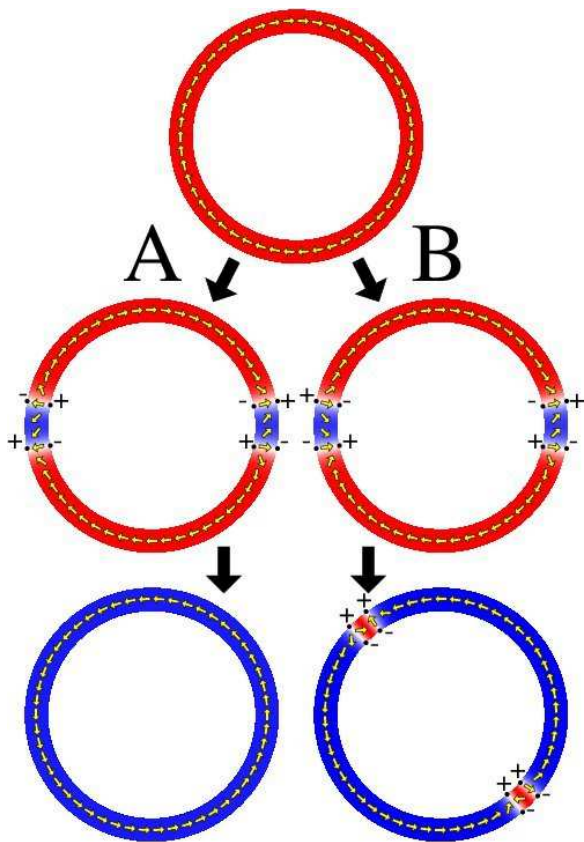


Figure 11: Two possible evolutions of a fluctuation with two instantons in different parts of the ring. (A) The magnetization relaxes to the metastable state only if the radial magnetization components are parallel. (B) Otherwise, two trapped domains (360 degree walls) appear.

Fig. 10 b). The field pushes the domain walls away from each other while their mutual interaction tends to bring them together. These opposing tendencies produce the unstable equilibrium which makes this configuration a saddle state.

The opposite situation, in which edge defects repel and the enclosed domain is antiparallel to the field, produces a metastable state. The enclosed magnetic domain does not vanish because the half vortices experience an effective repulsion: it is energetically costly to unwind the topological defects. As a result this configuration is stable, with an energy intermediate between the clockwise and counterclockwise configurations.

We can now explain how the metastable state evolves into the state represented in Fig. 10d. If the ring is originally magnetized clockwise, the energy density per ring segment of instanton fluctuation size is higher than the instanton energy. If the ring is sufficiently large, two instantons (one domain wall pair each) are produced (Fig. 11). If both instantons point in the same radial direction the system evolves into the counterclockwise state (Fig. 11 A). However, if the instanton fluctuations point in opposite radial directions (Fig. 11 B) the system evolves to

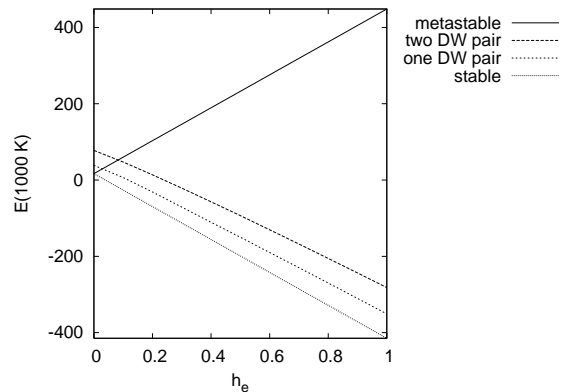


Figure 12: Spectra of large ring regime ($m \approx 1$). Lower metastable states are separated by the energy of a trapped domain configuration. Beyond the clockwise configuration the instanton saddle and the constant saddle are shown. The metastable configuration becomes unstable beyond $h_e = 1$.

the state shown with 4 domain walls .

The domain wall pairs need not be at opposite sides of the ring for this configuration to be stable, as confirmed by displacing one of the wall pairs by several angles and waiting for the system to relax.

It is interesting to summarize the new possible configurations and their total energies in the large ring case. The lowest state is the stable configuration, and there exists a series of metastable states separated from each other by the energy of a double wall trapped domain (Fig. 12)

With the exception of the single wall pair, all configurations shown have a total winding number difference from the counterclockwise state equal to zero for a path that completely encloses the central hole of the ring. The single wall pair configuration has this winding number difference equal to one. While reversing the field will make the double wall system decay into the stable state; the single wall pair configuration cannot decay into the counterclockwise configuration. A trapped domain configuration using a single pair of domain walls has already been proposed for an MRAM device²³.

VI. WIDE RINGS

Having verified numerically the conclusions and predictions of the analytical model of Martens et al.¹⁰ for narrow rings, we now proceed to test the limits of its applicability with increasing annular width. Given the 1D nature of the analytical mode, we expect that at some width the model should break down and its conclusions no longer apply. Surprisingly, this breakdown finally occurs at a larger width than initially expected.

Increasing the ring width introduces two new effects that cause the analytical model to break down. First, it allows the external field to vary in magnitude appreciably as one moves along a radial direction. Second, it

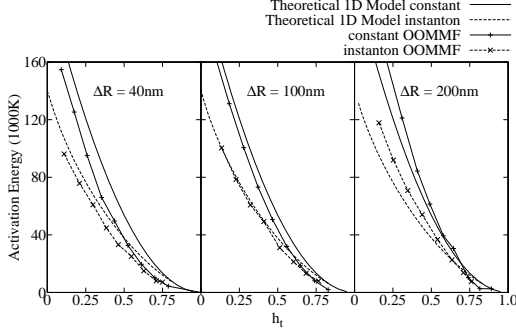


Figure 13: Activation energy spectra for $R = 200$ nm, $\ell = 12$ and a) $\Delta R = 40$ nm, b) 100 nm, c) 200 nm.

increases the relative magnitude of the (previously neglected) nonlocal bulk term of the magnetostatic energy with respect to that of the local surface term.

In our simulations, ΔR is set to the values 100 nm ($H_c = 29.5$ mT), 200 nm ($H_c = 14.7$ mT) and 380 nm ($H_c = 7.8$ mT). The central hole of the annulus is a few exchange lengths in diameter in the latter case. For this reason vortex-like “singularities” remain in the gap.

Fig. 13 summarizes the activation energies for the widths considered. It should be noticed that as ΔR increases for fixed λ , ℓ decreases and the annulus shifts away from the large ring ($m \approx 1$) approximation. We consequently discuss only middle size rings where $\ell \approx 12$. Fig. 13 a,b,c shows that the main predictions of the model hold even for very wide rings: the configurations ϕ_h are saddles for certain h_t , and for fields below h_c the instanton saddle configuration is preferred to the constant saddle configuration.

We have found that the annular width must be increased to the extreme wide-ring limit $\Delta R \approx 2R$ in order for the model to fail. Its breakdown can be observed in the $E(t)$ curve of Fig. 14a. In this regime, there are still fields h_t for which the dynamics bifurcates to either the stable or metastable state on either side of h_t , but at such fields it is clear from Fig. 14a that $(\lim_{h \rightarrow h_t} \frac{\delta E}{\delta t} |_{t=0} \neq 0^-)$. This indicates that the initial configurations chosen from the 1D analytical solutions are no longer close to the true saddles. Instead of a long initial period of little change, we find instead relaxation to a state in which the central region of the ring is magnetized circumferentially and the outer edge of the ring retains some memory of the starting configuration. This appears to be a new type of saddle configuration, which we call the *relaxed state*, and is shown in Fig. 14.

For simulations starting from the instanton saddle with parameters $h = 0.1, \dots, 0.4$ the system evolves to the relaxed state. At higher values of h ($h = 0.5, \dots, 0.8$ for the instanton, and $h = 0.7, \dots, 1.0$ for constant saddle configurations) the relaxed state does not satisfy the stationarity condition, but the bifurcation condition can still be satisfied with a particular h_t . The absence of a plateau

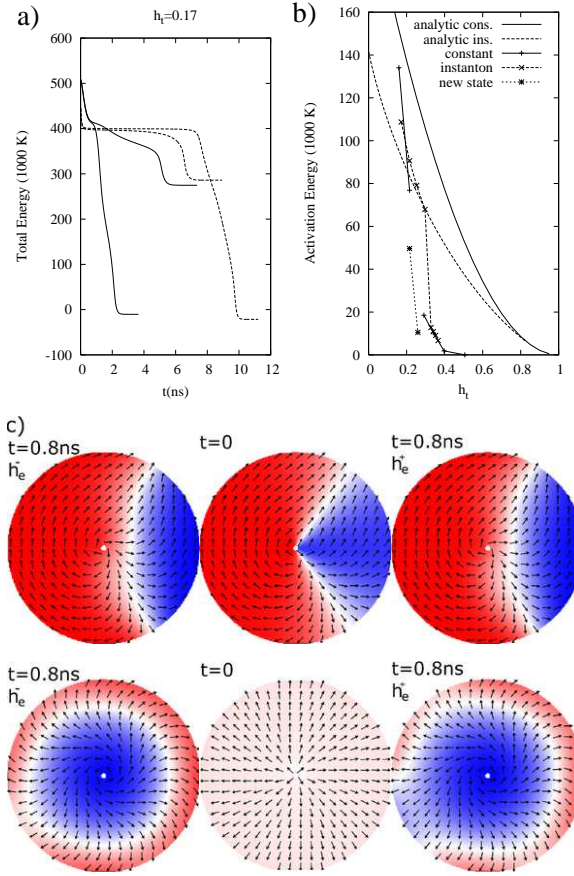


Figure 14: a) Time evolution of the total energy, for both initial saddle configurations. At a given h_t the dynamics do not slow arbitrarily as $t \rightarrow 0$. b) Spectra of the approximate activation energies (measured close to the bifurcation in time, not at $t = 0$). c) The new metastable state of Fig. 15 is found at lower energies than either saddle. The 1D saddle configurations (instanton center-up, constant center-down) and their corresponding relaxed states at $t=0.8$ ns for $(h_e^+$ right, h_e^- left); inside the ring the strong field aligns the magnetization clockwise .

in the E vs. t curves makes the definition of the activation energy somewhat more problematic, but it can still be defined by using as the energy of the saddle state the point at which the curves $E[\phi_h, h_e^-]$ and $E[\phi_h, h_e^+]$ separate. In this way approximate activation energy spectra can be determined, and the results are shown in Fig. 14b.

For values of h that correspond to the constant saddle ($0.2, \dots, 0.6$) another feature of the breakdown of the 1D model can be seen. The system relaxes to neither of the stable states considered so far (see Fig. 15). It evolves to a radially dependent state with counterclockwise orientation at the inner edge of the ring and clockwise orientation at the outer edge. This configuration is stabilized by the large inhomogeneity in the magnitude of the magnetic field as one moves outward along a radial direction. It is important to note that the energy of this state is lower than the energies of either initial configuration used (the

1D analytical saddle solutions), but is higher than either the clockwise or counterclockwise state.

There exists a low barrier that prevents this configuration from relaxing into either of the counterclockwise configurations in the limiting fields of Fig. 14. We obtain an estimate of this energy by using the String Method without reparametrization¹⁹ as described in Sect. III. We start with sequences of 50 equally spaced configurations that connect each of the circumferential configurations to this newly found metastable state along a straight line. The result of the relaxations are shown in Fig. 16. Fig. 16 (a) shows the total energy of the string points after relaxation; the inset shows a very shallow energy barrier that prevents decay to the two lowest stable configurations. It is interesting to observe that this barrier almost disappears on the left at $h_e = 0.22500$ and on the right at $h_e = 0.25625$ explaining why this state is stable only for a very narrow band of field values.

The physical origin of the two barriers is clear if the three components are studied separately (Fig. 16 b, c, d). For all graphs the origin corresponds to the state represented in Fig. 15, and the clockwise oriented magnetization is 50 steps to the left of zero, the counterclockwise configuration is located 50 steps to the right of zero.

The Zeeman energy (Fig. 16d) prevents the system from moving towards the clockwise configuration for all states along the string. It is maximum for the clockwise configuration and decreases monotonically along the path. Any point of the trajectory is pushed to the right of the graph by the external field.

Fig. 16b shows the demagnetization energy with a sharp barrier that prevents the magnetization from pointing perpendicular to the ring edges. At this barrier, the magnetization at the surface points radially outward (as in Fig. 14 h_e^+ for the constant saddle). This produces a sharp barrier at this step of the path. At this point, the magnetostatic energy is the only energy term acting against the reversal of the magnetization from clockwise to counterclockwise orientations; other terms favors the reversal. The net effect of the demagnetization energy barrier is to favor configurations away from this barrier. Fig. 16c represents the exchange energy. The exchange energy is minimal in the two circumferential states.

When these three interactions are considered together the stability of this state is understood: at lower fields the exchange and magnetostatic energy are balanced by the Zeeman energy. At large fields Zeeman and exchange favor a magnetization out of the ring's surface, when the shape anisotropy barrier is overcome, the system reverses suddenly into the counterclockwise configuration.

The analytical model presumed the field to be constant in the radial direction as in the narrow ring case. Although the field inhomogeneity eventually renders this assumption invalid, the 1D model is surprisingly robust and breaks down only in the extreme case just considered.

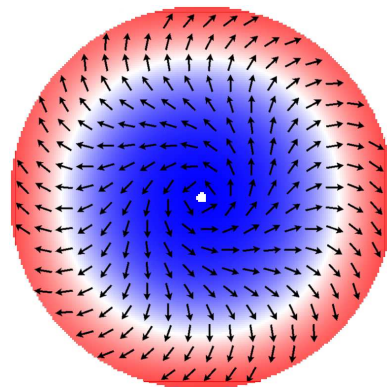


Figure 15: Magnetization configuration of new found metastable state for extremely wide rings. The stability of this state is a consequence of the highly inhomogeneous field in the center.

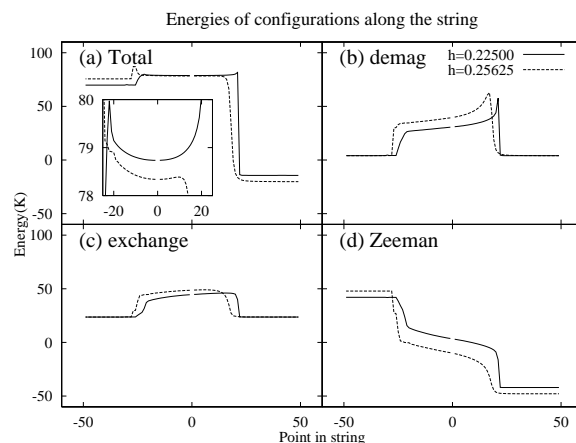


Figure 16: Energies of the configurations along the string after 100 iterations at two different applied fields. The center of the figure represents the magnetization configuration of Fig. 15. The clockwise configuration is at -50, and the counterclockwise is located at +50. Energies are a) total b) demagnetization c) exchange d) Zeeman. The inset on (a) shows the energy on a finer scale, illustrating the existence of an energy barrier.

VII. CONCLUSION

The 1D analytical model of Martens *et al.*¹⁰ has been tested and confirmed using numerical simulations for a variety of ring sizes and external magnetic fields that more closely approximate realistic laboratory situations. Although it was initially expected that the analytical model would apply only to narrow annuli, our simulations show that it is surprisingly robust, eventually breaking down only in the extreme two-dimensional limit.

By studying a large portion of the relevant parameter space, $(\lambda, \Delta R)$, we have also found new saddle and stable states. These findings enrich our understanding of the energy landscape of ferromagnetic rings.

Two limits present particularly interesting features: the large- R narrow ring ($\Delta R \ll R$) and the extremely

wide ring. The large narrow ring allows for the appearance of multiple instantons at energies below the constant saddle configuration; their relative orientations and positions determine the final magnetization configuration. We provide a topological analysis of these new configurations and predict a hierarchy of such states differing by the number of domain wall pairs in each. The interaction between these domain walls can be characterized and understood through “edge defects” that compose them. Moreover, by following the evolution of the downhill energy run from one of these states to the stable configuration, one can infer the propagation of domain wall pairs in the ring: sudden changes in energy indicate annihilation of domain wall pairs, while linear decrease of energy occurs during domain wall propagation.

The 1D model predicts extremely well the activation energy for magnetization reversal even for wide rings. Eventually, though, in the extremely wide regime limit, the 2D nature of the magnetic field becomes important and the 1D approximation breaks down. In this regime, a new stable state arises in which the magnetization is

radially dependent but independent of the angle. The String Method¹⁹ has been used to verify the existence of a barrier between this state and other stable states with lower energy, and is used to clarify the physical origin of this barrier, in terms of the various contributions to the energy from exchange, magnetostatic, and external field sources.

Acknowledgments

We want to thank Hans Fangohr for providing assistance in the use of the Nmag simulation package. We also acknowledge Daniel Bedau for helpful insight. This research has been partially supported by NSF-DMR-0706322 and an NYU-Research Challenge Fund award (ADK) and by NSF-PHYS-0651077 (DLS). We are grateful to Oleg Tretiakov for commenting on the first draft of this manuscript.

-
- [1] C. L. Chien, F. Zhu, and J.G.Zhu, *Phys. Today* **60**, 40 (2007).
- [2] T. Yang, M. Hara, A. Hirohata, T. Kimura, and Y. Otani, *Appl. Phys. Lett.* **90**, 022504 (2007).
- [3] J.-G. Zhu, Y. Zheng, and G. A. Prinz, in *J. Appl. Phys.* (AIP, 2000), vol. 87, pp. 6668–6673.
- [4] M. Kläui, Vaz, J. A. C. Bland, T. L. Monchesky, J. Unguris, E. Bauer, S. Cherifi, S. Heun, A. Locatelli, L. J. Heyderman, et al., *Phys. Rev. B* **68**, 134426 (2003).
- [5] M. Kläui, C. A. F. Vaz, J. A. C. Bland, L. J. Heyderman, F. Nolting, A. Pavlovskaja, E. Bauer, S. Cherifi, S. Heun, and A. Locatelli, *Appl. Phys. Lett.* **85**, 5637 (2004).
- [6] M. Laufenberg, D. Backes, W. Buhner, D. Bedau, M. Kläui, U. Rudiger, C. A. F. Vaz, J. A. C. Bland, L. J. Heyderman, F. Nolting, et al., *Appl. Phys. Lett.* **88**, 052507 (2006).
- [7] F. J. Castaño, C. A. Ross, C. Frandsen, A. Eilez, D. Gil, H. I. Smith, M. Redjda, and F. B. Humphrey, *Phys. Rev. B* **67**, 184425 (2003).
- [8] F. J. Castaño, D. Morecroft, and C. A. Ross, *Physical Rev. B (Condensed Matter and Materials Phys.)* **74**, 224401 (2006).
- [9] J. Rothman, M. Kljœui, L. Lopez-Diaz, C. A. F. Vaz, A. Bleloch, J. A. C. Bland, Z. Cui, and R. Speaks, *Phys. Rev. Lett.* **86**, 1098 (2001).
- [10] K. Martens, D. L. Stein, and A. D. Kent, *Phys. Rev. B (Condensed Matter and Materials Phys.)* **73**, 054413 (2006).
- [11] G. D. Chaves-O’Flynn, K. Xiao, D. L. Stein, and A. D. Kent, *J. Appl. Phys.* **103**, 07D917 (2008).
- [12] H. A. Kramers, *Physica* **7**, 284 (1940).
- [13] P. Hänggi, P. Talkner, and M. Borkovec, *rev. of Modern Phys.* **62**, 251 (1990).
- [14] T. L. Gilbert, *Phys. Rev.* **100**, 1243 (1955).
- [15] L. Landau and E. Lifshitz, *Physik. Z* **8**, 152 (1935).
- [16] M. Abramowitz and I. A. Stegun (Dover Publications, 1965), ISBN 0486612724.
- [17] M. Donahue and D. Porter, National Institute of Standards and Technology, Gaithersburg, MD, version 1.0 ed. (1999).
- [18] T. Fischbacher, M. Franchin, G. Bordignon, and H. Fangohr, *Magnetics*, *IEEE Transactions on* **43**, 2896 (2007).
- [19] W. E. W. Ren, and E. Vanden-Eijnden, *Phys. Rev. B* **66**, 052301 (2002).
- [20] H.-B. Braun, *Phys. Rev. Lett.* **71**, 3557 (1993).
- [21] P. M. Chaikin and T. C. Lubensky (Cambridge University Press, 2000), 1st ed., ISBN 0521794501.
- [22] O. Tchernyshyov and G.-W. Chern, *Phys. Rev. Lett.* **95**, 197204 (2005).
- [23] M. Moneck and J.Zhu (2007), no. 52nd in Annual Conference on Magnetism and Magnetic Materials, MMM.